Towards optimal and robust $f_{\rm NL}$ constraints with multi-tracer analyses

Alexandre Barreira a,b and Elisabeth Krause c

E-mail: alex.barreira@origins-cluster.de, krausee@arizona.edu

Abstract. We discuss the potential of the multi-tracer technique to improve observational constraints of the local primordial non-Gaussianity (PNG) parameter $f_{\rm NL}$ from the galaxy power spectrum. For two galaxy samples A and B, the constraining power is $\propto |b_1^B b_\phi^A - b_1^A b_\phi^B|$, where b_1 and b_ϕ are the linear and PNG galaxy bias parameters. We show this allows for significantly improved constraints compared to the traditional expectation $\propto |b_1^A - b_1^B|$ based on naive universality-like relations where $b_\phi \propto b_1$. Using IllustrisTNG galaxy simulation data, we find that different equal galaxy number splits of the full sample lead to different $|b_1^B b_\phi^A - b_1^A b_\phi^B|$, and thus have different constraining power. Of all of the strategies explored, splitting by g-r color is the most promising, more than doubling the significance of detecting $f_{\rm NL}b_\phi \neq 0$. Importantly, since these are constraints on $f_{\rm NL}$, we show that multi-tracer constraints can be significantly more robust than single-tracer to b_ϕ misspecifications and uncertainties; this relaxes the precision and accuracy requirements for b_ϕ priors. Our results present new opportunities to improve our chances to detect and robustly constrain $f_{\rm NL}$, and strongly motivate galaxy formation simulation campaigns to calibrate the $b_\phi(b_1)$ relation.

^aExcellence Cluster ORIGINS, Boltzmannstraße 2, 85748 Garching, Germany

 $[^]b$ Ludwig-Maximilians-Universität, Schellingstraße 4, 80799 München, Germany

^cDepartment of Astronomy and Steward Observatory, University of Arizona, 933 North Cherry Ave, Tucson, Arizona 85721, USA

Contents

1	Introduction 2 Fisher information analysis			
2				
	2.1 Single-tracer case	2		
	2.2 Multi-tracer case			
	2.3 Simple illustration of the impact of galaxy bias	3		
3	Multi-tracer examples from galaxy formation simulations			
	3.1 Simulated galaxy samples	4		
	3.2 Constraints for the simulated galaxy samples	(
4	The impact of priors on b_{ϕ}	6		
	4.1 The impact of systematic offsets in b_{ϕ}	7		
	4.2 Exploration of multi-tracer b_{ϕ} prior requirements	8		
5	Summary and Conclusions	9		
\mathbf{A}	Derivation of the Fisher information content in multi-tracer analyses	10		

1 Introduction

Constraining the local primordial non-Gaussianity (PNG) parameter $f_{\rm NL}$ [1] is one of the most powerful ways to learn about the physics of inflation. A detection of $f_{\rm NL} \neq 0$ could rule out single-field inflation [2–6], and constraining $|f_{\rm NL}| \lesssim 1$ can be used to test many other classes of models [7–9]. The current tightest bound is $f_{\rm NL} = -0.9 \pm 5.1 \ (1\sigma)$ from cosmic microwave background data [10], and the next improvements over it are expected to come from galaxy clustering analyses [7–9].

In local PNG cosmologies, the linear galaxy density contrast contains two terms given by [11–15]

$$\delta_q(\mathbf{k}, z) \supset b_1(z)\delta_m(\mathbf{k}, z) + b_\phi(z)f_{\rm NL}\phi(\mathbf{k}),$$

$$\tag{1.1}$$

where k is the wavevector, δ_m is the matter density contrast, ϕ is the primordial potential in the matter era, and b_1 and b_{ϕ} are galaxy bias parameters that describe the response of galaxy formation to large-scale δ_m and ϕ perturbations, respectively [16]. The contribution from $f_{\rm NL}$ in Eq. (1.1) is called the scale-dependent bias effect [17], and is how galaxy data are most directly sensitive to $f_{\rm NL}$. Some of the latest reported constraints using galaxy data include $f_{\rm NL} = -12 \pm 21$ (1 σ) using eBOSS quasars [18] (see also Ref. [19]), and $f_{\rm NL} = -30 \pm 29$ (1 σ) [20] and $f_{\rm NL} = -33 \pm 28$ (1 σ) [21] using galaxies in the BOSS survey. Note however that these constraints require knowledge of the $b_{\phi}(b_1)$ relation to break the $f_{\rm NL}b_{\phi}$ degeneracy in Eq. (1.1). This relation is still uncertain [22–28], and so these bounds on $f_{\rm NL}$ are currently subject to significant model systematic errors [29, 30]; independently of b_{ϕ} , only the parameter combination $f_{\rm NL}b_{\phi}$ can be robustly constrained, and not $f_{\rm NL}$

The multi-tracer technique [31] is a tool to increase the statistical constraining power of a given galaxy sample. The idea is to split the galaxy sample into sub-samples occupying the same volume. Since the sub-samples formed from the same initial density field, at sufficiently high number density, the relative clustering amplitude of the sub-samples can be measured effectively noise-free and can be used to constrain $f_{\rm NL}$ with very high precision (see Refs. [32, 33] for recent studies of the impact of multi-tracer analyses to constrain other cosmological parameters). In doing so, relations like the universality relation $b_{\phi}(b_1) = 2\delta_c(b_1 - 1)$, $\delta_c = 1.686$, where b_1 and b_{ϕ} vary proportionally to each other are traditionally assumed in $f_{\rm NL}$ constraints, which for multi-tracer analyses leads to the constraining power being maximized for large differences in b_1 of the sub-samples. However, a number of recent works using galaxy formation simulations [24–27] have shown that these universality-based relations are likely not good descriptions of real-life galaxies, making it interesting to revisit this expectation.

In this paper we use the possibility that different galaxy types may have different $b_{\phi}(b_1)$ relations to investigate optimal galaxy selection strategies for $f_{\rm NL}$ multi-tracer constraints. For splits into two sub-samples A and B, the constraining power is $\propto |b_1^B b_{\phi}^A - b_1^A b_{\phi}^B|$ [31], and not simply $\propto |b_1^A - b_1^B|$ as when naively assuming the universality relation. That is, the constraining power is the greatest for multi-tracer splits in which b_{ϕ} and b_1 vary inversely proportional to each other, which is orthogonal to the case enforced by the universality relation. Interestingly, using galaxy formation simulations, we are able to identify multi-tracer splits, e.g. based on galaxy color, that can have large values of $|b_1^B b_{\phi}^A - b_1^A b_{\phi}^B|$ and thus exploit much better the power of the multi-tracer technique to detect $f_{\rm NL} \neq 0$.

We also investigate the impact that b_{ϕ} priors have in multi-tracer analyses. Compared to single-tracer, we find that multi-tracer analyses are more robust to $f_{\rm NL}$ biases due to b_{ϕ} misspecifications, as well as degradation in $f_{\rm NL}$ constraining power due to b_{ϕ} uncertainties. This motivates further investing in the multi-tracer technique in $f_{\rm NL}$ constraints as a way to relax the accuracy and precision requirements on b_{ϕ} priors calibrated from galaxy formation simulations.

The rest of this paper is as follows. In Sec. 2 we study the impact that b_1 and b_{ϕ} have on the $f_{\rm NL}$ Fisher information in single- and multi-tracer cases. In Sec. 3 we show the improvements in $f_{\rm NL}$ constraints from multi-tracer analyses using galaxies from hydrodynamical simulations. We investigate the robustness of single- and multi-tracer constraints to priors on b_{ϕ} in Sec. 4, and conclude in Sec. 5.

For all numerical results we assume a fictitious galaxy survey at z=1 with volume $V_S=100~{\rm Gpc^3}/h^3$, and consider multi-tracer splits into two sub-samples A,B with equal number density, i.e. $\bar{n}_g^A=\bar{n}_g^B=\bar{n}_g/2$. We assume the spectra is measured from $k_{\rm min}=\pi/V_S^{1/3}$ up to $k_{\rm max}=0.2h/{\rm Mpc}$ in 40 log-spaced k bins. We adopt the following cosmological parameters throughout: $\Omega_m=0.3089$, $\Omega_b=0.0486$, $\Omega_\Lambda=0.6911$, $H_0=100h~{\rm km/s/Mpc}$ with h=0.6774, $n_s=0.967$, $\sigma_8=0.816$ and $f_{\rm NL}=5$. We note our main conclusions do not change under reasonable modifications to any of these values. We use the CAMB code [34] to calculate power spectra and transfer functions.

2 Fisher information analysis

In this section, we discuss the impact that different values of the galaxy bias parameters b_1 and b_{ϕ} have on the f_{NL} Fisher information.

2.1 Single-tracer case

The large-scale power spectrum of a single galaxy sample can be written in real space as

$$P_{gg}(k,z) = \left[b_1(z) + b_{\phi}(z) f_{\text{NL}} \mathcal{M}(k,z)^{-1} \right]^2 P_{mm}(k,z) + P_{\epsilon}, \tag{2.1}$$

where P_{mm} is the linear matter power spectrum and $P_{\epsilon} = 1/\bar{n}_g$ is the shot noise (which we assume Poissonian). The quantity \mathcal{M} is defined as $\delta_m(\mathbf{k},z) = \mathcal{M}(k,z)\phi(\mathbf{k})$, and given by $\mathcal{M}(k,z) = (2/3)k^2T_m(k)D_{\mathrm{md}}(z)/(\Omega_mH_0^2)$, where T_m is the matter transfer function and D_{md} is the linear growth factor normalized to 1/(1+z) during matter domination. The Fisher information on f_{NL} is

$$F_{f_{\rm NL}}(k,z) = \frac{\partial P_{gg}(k,z)}{\partial f_{\rm NL}} \text{Cov}^{-1}(k,z) \frac{\partial P_{gg}(k,z)}{\partial f_{\rm NL}}, \tag{2.2}$$

where Cov is the data covariance matrix. As we focus on f_{NL} constraints, which are dominated by the largest scales, we approximate the covariance by the diagonal disconnected component

$$Cov(k,z) = \frac{2(2\pi)^3}{V_S V_k} P_{gg}(k,z)^2,$$
(2.3)

where V_S is the survey volume, $V_k = 4\pi k^2 \Delta k$, and Δk is the wavenumber bin size; from hereon we suppress the redshift dependence to ease the notation.

The error bar on $f_{\rm NL}$ is given by $\sigma_{f_{\rm NL}} = 1/\sqrt{F_{f_{\rm NL}}}$, which reads as

$$\sigma_{f_{\rm NL}}(k) = \sqrt{\frac{2(2\pi)^3}{V_S V_k}} \frac{b_1 + b_\phi f_{\rm NL} \mathcal{M}(k)^{-1}}{2b_\phi \mathcal{M}(k)^{-1}} (1 + X(k)), \qquad (2.4)$$

where we introduced $X(k) = P_{\epsilon}/(P_{gg}(k) - P_{\epsilon})$ to quantify the impact of shot noise. Concerning the bias parameters, this expression tells us that the constraining power on $f_{\rm NL}$ increases with larger values of b_{ϕ} . This is for two reasons. First, at fixed number density \bar{n}_g , increasing b_{ϕ} lowers X, which decreases $\sigma_{f_{\rm NL}}$. Second, the precision on $f_{\rm NL}$ increases also if $b_{\phi} \gg b_1$ as the Gaussian contribution to the power spectrum $\propto b_1^2$ does not contain information on $f_{\rm NL}$, but still contributes to the total variance in Eq. (2.3); i.e., the limit $b_{\phi} \gg b_1$ maximizes the signal-to-noise on $f_{\rm NL}$. This is the idea explored in Ref. [35] with zero-bias tracers in which one attempts to select a galaxy sample with $b_1 = 0$ that suffers only from a cosmic variance error given by

$$\sigma_{f_{\rm NL}}(k) = \sqrt{\frac{2(2\pi)^3}{V_S V_k}} \frac{f_{\rm NL}}{2} \left(1 + X(k)\right). \tag{2.5}$$

The takeaway for single-tracer analyses is thus that, at fixed number density \bar{n}_g , the optimal $f_{\rm NL}$ constraints are obtained with samples that have the largest values of b_{ϕ} and the lowest values of b_1 .

2.2 Multi-tracer case

We consider multi-tracer analyses in which a full galaxy sample is split into two equal-sized subsamples labeled as A and B. The data vector is now composed of the power spectra and cross-spectra of the two samples $\mathbf{D}(k) = \left\{ P_{gg}^A(k), P_{gg}^{A \times B}(k), P_{gg}^B(k) \right\}$, and the Fisher information is

$$F_{f_{NL}}(k) = \frac{\partial \mathbf{D}^{t}(k)}{\partial f_{NL}} \cdot \mathbf{Cov}^{-1}(k) \cdot \frac{\partial \mathbf{D}(k)}{\partial f_{NL}}, \tag{2.6}$$

where $\mathbf{Cov}(k)$ is the covariance of the data vector \mathbf{D} (cf. Eq. (A.3)). In the cosmic variance limit $X^A, X^B \ll 1$, the result is given by (we outline a few intermediate steps of the derivation in App. A)

$$F_{f_{NL}} = 2 \frac{V_S V_k}{2(2\pi)^3} \frac{1}{X^B + X^A} \left(\frac{\left(b_1^B b_\phi^A - b_1^A b_\phi^B \right) \mathcal{M}(k)^{-1}}{R \left(b_1^B + f_{NL} b_\phi^B \mathcal{M}(k)^{-1} \right)^2} \right)^2 + \mathcal{O}\left(X^A, X^B\right), \tag{2.7}$$

where $R = (P_{gg}^B - P_{\epsilon}^B)/(P_{gg}^A - P_{\epsilon}^A)$, and the superscripts label the various quantities for samples A and B; for example $X^A = P_{\epsilon}^A/(P_{gg}^A - P_{\epsilon}^A)$. One of the important impacts of galaxy bias comes through the value of $|b_b^B b_\phi^A - b_b^A b_\phi^B|$ in the numerator of Eq. (2.7); this is as previously derived in Ref. [31] (see their Eq. (10)). Effectively all works in the literature assume the universality relation $b_\phi(b_1) = 2\delta_c(b_1 - 1)$ (or some variant of it with $b_\phi \propto b_1$), from which it follows that $F_{f_{\rm NL}}$ increases with increasing $|b_1^A - b_1^B|$. This is why multi-tracer analyses were traditionally described as having greater constraining power when the sub-samples have very different b_1 . In this paper, however, we highlight that the situation is actually richer than what universality naively suggests: in the limit of low shot noise, the precision on $f_{\rm NL}$ increases with increasing $|b_1^B b_\phi^A - b_1^A b_\phi^B|$, and not just $|b_1^A - b_1^B|$.

This is interesting as a number of studies [22–28] have found using simulations that the $b_{\phi}(b_1)$ relation is a very sensitive function of the details of halo and galaxy formation physics. Thus, provided we are able to understand the $b_{\phi}(b_1)$ relation of real galaxies sufficiently well, this gives us a chance to optimize our galaxy selection strategies by exploring cases that maximize the parameter combination $|b_1^B b_{\phi}^A - b_1^A b_{\phi}^B|$. Indeed, as we will see throughout, this can lead to significant improvements compared to the traditional expectation based on the universality relation.

2.3 Simple illustration of the impact of galaxy bias

Figure 1 compares the constraining power of different values of b_1 and b_{ϕ} in multi-tracer $f_{\rm NL}$ constraints. In this toy illustration we place the sub-samples A and B on a unit circle centered around the b_1 and b_{ϕ} values of the full sample, with each A, B sample pair linking diametrically opposed points. The values of the full sample are $b_1 = 2$ and $b_{\phi} = 2\delta_c(b_1 - 1) = 3.37$. The left panel shows the result for

¹This can be seen also as the $f_{\rm NL}$ precision being $\propto \sin \alpha$, with α the angle between the vectors (b_1^A, b_{ϕ}^A) and (b_1^B, b_{ϕ}^B) .

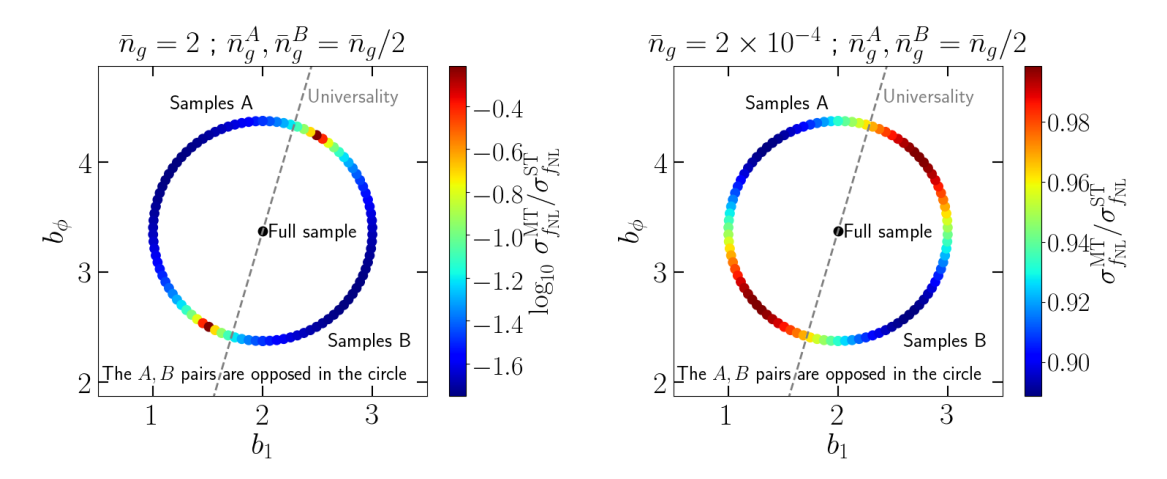


Figure 1. Relative improvement in $f_{\rm NL}$ constraints for different values of b_1 and b_{ϕ} in multi-tracer (MT) analyses. The pairs of galaxy sub-samples are chosen to be diametrically opposed on a unit radius circle around the full sample values $b_1 = 2$ and $b_{\phi} = 3.37$. Concretely, $b_1^B = b_1 + \cos(\theta)$, $b_{\phi}^B = b_{\phi} + \sin(\theta)$ and $b_1^A = b_1 + \cos(\theta + \pi)$, $b_{\phi}^A = b_{\phi} + \sin(\theta + \pi)$, with $\theta \in [-\pi/2, \pi/2]$; this simple parametrization serves only the purpose to illustrate the typical impact of b_1 and b_{ϕ} . The result is for equal number density splits $\bar{n}_g^A = \bar{n}_g^B = \bar{n}_g/2$; the left and right panels are for an unrealistically large and realistic value of n_g , as labeled (the \bar{n}_g units are $h^3/{\rm Mpc}^3$). The colors indicate the improvement of the multi-tracer constraints relative to the single-tracer (ST) result using the full galaxy sample. The grey dashed line shows the universality relation.

an unrealistically large value of the number density $\bar{n}_g = 2 \ h^3/{\rm Mpc^3}$ to enforce the cosmic variance limited regime, and the right panel shows the result for a realistic value of $\bar{n}_g = 2 \times 10^{-4} \ h^3/{\rm Mpc^3}$.

In the cosmic variance limit on the left of Fig. 1, the improvement is largest (dark blue) when the b_1 and b_{ϕ} values of the sub-samples vary inversely proportional to each other. This is as expected from Eq. (2.7) since this is what maximizes the $|b_1^B b_{\phi}^A - b_1^A b_{\phi}^B|$ factor. Conversely, when $|b_1^B b_{\phi}^A - b_1^A b_{\phi}^B| \approx 0$, the improvements from the multi-tracer technique become much less pronounced (cf. red and yellow points on the left). Further, the grey dashed line shows the universality relation, which is not aligned with the directions in the $b_1 - b_{\phi}$ plane that give the best constraints.

For the realistic number density scenario on the right of Fig. 1, the $\mathcal{O}\left(X^A,X^B\right)$ terms in Eq. (2.7) spoil the exact scaling with $|b_1^B b_{\phi}^A - b_1^A b_{\phi}^B|$, but the qualitative picture remains the same: there is still a correlation between the improvement of the constraints and the value of $|b_1^B b_{\phi}^A - b_1^A b_{\phi}^B|$, which happens for directions in the $b_1 - b_{\phi}$ that are orthogonal to the universality direction. Note that the quantitative improvements in Fig. 1 are specific to our illustrative choice of bias parameters; below we discuss results for more realistic values of b_1 and b_{ϕ} .

3 Multi-tracer examples from galaxy formation simulations

In the last section we have identified that multi-tracer analyses that maximize the value of $|b_1^B b_{\phi}^A - b_1^A b_{\phi}^B|$ are those that return optimal constraints on $f_{\rm NL}$. What we wish to do now using galaxy formation simulations is to identify which galaxy selection strategies can lead to larger values of $|b_1^B b_{\phi}^A - b_1^A b_{\phi}^B|$, and are thus optimal to constrain $f_{\rm NL}$ using the multi-tracer technique.

3.1 Simulated galaxy samples

We utilize the N-body simulation data of Refs. [24, 26], concretely a suite of gravity-only and galaxy formation simulations run with the IllustrisTNG galaxy formation model [36]. We refer the reader to Refs. [24, 26] (as well as to Ref. [28]) for the details about how the b_1 and b_{ϕ} parameters are measured using the separate universe approach.

We will show results for galaxy samples constructed as follows. The full galaxy sample is obtained by applying a minimum total mass cut at z=1 that yields a total number density of $\bar{n}_q=2$ ×

	M_t	M_*	g-r	$\dot{M}_{ m BH}$	$n_{g,8}$	c_{200} (halos)
$\left(b_1^A, b_1^B\right)$	(3.0, 2.5)	(3.0, 2.5)	(2.8, 2.7)	(3.2, 2.2)	(5.4, 0.1)	(2.4, 3.0)
$\left(b_{\phi}^{A},b_{\phi}^{B} ight)$	(5.0, 3.9)	(7.3, 1.6)	(9.1, -0.2)	(4.3, 4.7)	(9.1, -0.1)	(6.9, 3.6)
$ b_1^B b_\phi^A - b_1^A b_\phi^B $	0.5	13.5	25.0	5.5	1.4	11.6

Table 1. Numerical values of b_1 and b_{ϕ} of the simulated galaxy samples used in this work. The columns for M_t , M_* , g-r, $\dot{M}_{\rm BH}$ and $n_{g,8}$ are for splits of a galaxy sample with $b_1=2.7$ and $b_{\phi}=4.5$. The column for c_{200} is for a split of a halo sample with $b_1=2.7$ and $b_{\phi}=5.3$. All samples are at z=1 and the full sample has $\bar{n}_g=2\times 10^{-4}~h^3/{\rm Mpc}^3$. All splits are at equal number density $\bar{n}_g^A=\bar{n}_g^B=\bar{n}_g/2$ using the 50% highest (sample A) and lowest (sample B) values of each property. The last line lists the parameter combination $|b_1^Bb_{\phi}^A-b_1^Ab_{\phi}^B|$ that controls the constraining power of multi-tracer analyses on $f_{\rm NL}$ (cf. Eq. (2.7)).

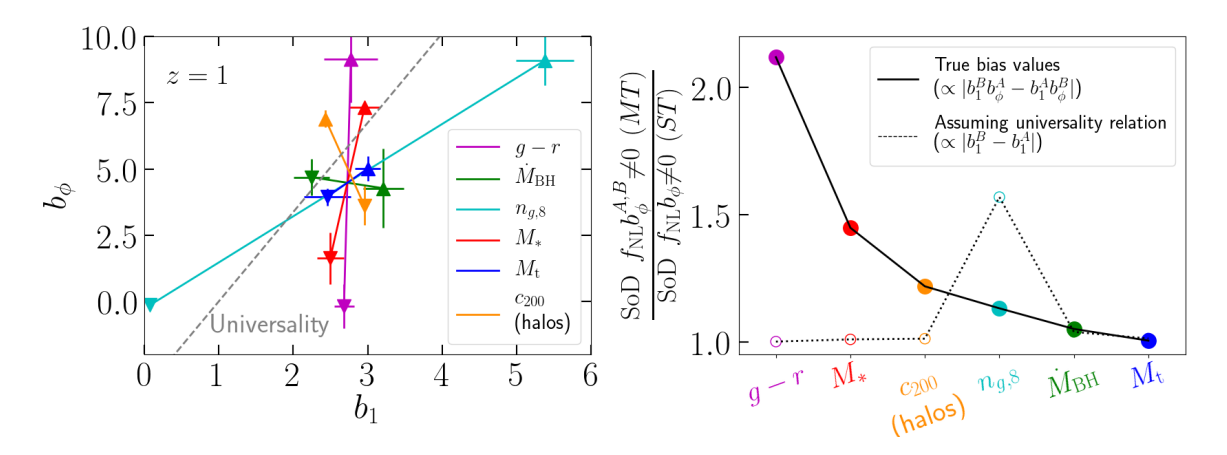


Figure 2. Improvements on the significance of detection (SoD) of $f_{\rm NL} \neq 0$ for several equal-number multitracer (MT) splits using halos and galaxies in simulations. The full sample is obtained with a minimum total mass cut that results in $\bar{n}_g = 2 \times 10^{-4} \ h^3/{\rm Mpc}^3$ at z=1. The two sub-samples are constructed by splitting this sample in half according to the values of different galaxy properties, as labeled: total mass M_t , stellar mass M_* , g-r color, black hole mass accretion rate $\dot{M}_{\rm BH}$, and environmental density $n_{g,8}$. The resulting b_1 and b_{ϕ} values are marked on the left panel and in Tab. 1. The solid line and filled symbols in the right panel show the improvement on the significance-of-detection (SoD) of $f_{\rm NL}$ relative to single-tracer (ST) from Fisher forecasts for a survey with $V_S = 100 \ {\rm Gpc}^3/h^3$ at z=1. The dotted line and open symbols show the same but assuming the universality relation to highlight the gains from taking into account the true bias parameters.

 $10^{-4}~h^3/{\rm Mpc}^3.^2$ This sample is then split into two sub-samples that have the 50% lowest and highest values of different galaxy properties. We consider splits by: (i) total mass M_t , (ii) stellar mass M_* , (iii) g-r color, (iv) black hole mass accretion rate $\dot{M}_{\rm BH}$ and (v) environmental density $n_{g,8}$, defined as the number density of neighbour galaxies within 8 Mpc/h, which we estimate using the method of Ref. [37]. In addition, we consider also a main halo population constructed in the same way, but split into two by their Navarro-Frenk-White c_{200} concentration [28]. Our halo results are for a gravity-only simulation with $L_{\rm box}=560~{\rm Mpc}/h$ and $N_p=1250^3$ tracer particles, while our galaxy results are for simulations with IllustrisTNG with $L_{\rm box}=205~{\rm Mpc}/h$ and $N_p=2\times1250^3$. The cosmology of these simulations is the same as that adopted in this paper, except that $f_{\rm NL}=0$ (cf. Sec. 1).

The left panel of Fig. 2 shows the b_1 and b_{ϕ} values of all these samples, as labeled; they are also listed in Tab. 1. The value for the full sample is identified by where all lines intercept (except the orange one for c_{200}). The orange line for c_{200} for halos does not intersect the same point because the full halo population has slightly different bias values compared to the full galaxy sample. A remarkable aspect of the result is that different ways to split the same galaxy sample into two equal

²We have repeated the analysis for z=0,0.5,1,2,3, as well as for higher $(\bar{n}_g=5\times 10^{-4}~h^3/{\rm Mpc^3})$ and lower $(\bar{n}_g=1\times 10^{-4}~h^3/{\rm Mpc^3})$ number densities, and found qualitatively consistent results. Analyses with a full sample selected by a minimum stellar mass cut revealed also the same main takeaway points.

number density sub-samples can shift the bias parameters in markedly different directions in the $b_1 - b_{\phi}$ plane. That is, at least within the astrophysics of the IllustrisTNG model, there is indeed room to explore different galaxy selection strategies to optimize multi-tracer $f_{\rm NL}$ constraints.

3.2 Constraints for the simulated galaxy samples

The solid line and filled symbols in the right panel of Fig. 2 show the ratio of the significance of detection (SoD) of $f_{\rm NL} \neq 0$ for the various multi-tracer splits and the single-tracer result with the full sample. Concretely, we use a Fisher forecast to constrain the parameter combination $f_{\rm NL}b_{\phi}$, which lets us assess the SoD without priors on b_{ϕ} . Note that detecting $f_{\rm NL}b_{\phi} \neq 0$ implies $f_{\rm NL} \neq 0$, so it is still possible to learn something about inflation (namely that it was not single-field) without knowing the actual value of $f_{\rm NL}$. To date, the only examples of constraints placed directly on $f_{\rm NL}b_{\phi}$ were obtained in Refs. [21, 30] using BOSS DR12 galaxies. For single-tracer analyses, the SoD is defined as ${\rm SoD}^{\rm ST} = \langle f_{\rm NL}b_{\phi}\rangle/\sigma_{f_{\rm NL}}b_{\phi}$, where $\langle f_{\rm NL}b_{\phi}\rangle$ and $\sigma_{f_{\rm NL}b_{\phi}}$ are the mean of the constraints and the 1σ error bar, respectively. For multi-tracer samples, the SoD is given by

$$SoD^{MT} = \sqrt{\left(\langle f_{NL}b_{\phi}^{A}\rangle, \langle f_{NL}b_{\phi}^{B}\rangle\right)^{t} \cdot F_{f_{NL}b_{\phi}^{A}, f_{NL}b_{\phi}^{B}} \cdot \left(\langle f_{NL}b_{\phi}^{A}\rangle, \langle f_{NL}b_{\phi}^{B}\rangle\right)},$$
(3.1)

where $\langle f_{\rm NL}b_\phi^A\rangle$ and $\langle f_{\rm NL}b_\phi^B\rangle$ are the mean of the constraints and $F_{f_{\rm NL}b_\phi^A,f_{\rm NL}b_\phi^B}$ is their Fisher matrix.

The result in Fig. 2 shows that the choice of multi-tracer strategy can have a significant impact on the SoD of $f_{\rm NL} \neq 0$. The corresponding values of $|b_1^B b_{\phi}^A - b_1^A b_{\phi}^B|$ are listed in Tab. 1, which display the expected correlation with the improvement of the SoD from Eq. (2.7). The only exception is the split by $\dot{M}_{\rm BH}$, which performs worse than $n_{g,8}$, despite the larger $|b_1^B b_{\phi}^A - b_1^A b_{\phi}^B|$; this is because the $|b_1^B b_{\phi}^A - b_1^A b_{\phi}^B|$ scaling in Eq. (2.7) is only exact in the cosmic variance limit. Of all the multi-tracer cases considered, the split by g - r color performs the best, more than doubling the SoD of $f_{\rm NL}$ compared to single-tracer.³ We emphasize that these improvements can normally be achieved for free if galaxy imaging data exist, i.e. they do not require additional spectroscopic observations.

In order to highlight the differences to the traditional approach in the literature, the dotted line and open symbols show the same, but incorrectly assuming that b_{ϕ} is determined from b_1 using the universality relation. The differences are significant, strongly motivating abandoning assuming the universality relation in multi-tracer $f_{\rm NL}$ constraints. In particular, the universality expectation $\propto |b_1^A - b_1^B|$ misleadingly characterizes the g - r multi-tracer split as very weak, despite it being the best in this work. Conversely, the two $n_{g,8}$ samples have the largest difference in b_1 , and so are misleadingly classified as being the best multi-tracer split, despite it being actually one of the worst.

We stress also that the improvements in the SoD in Fig. 2 can be pursued even without accurate calibration of the b_{ϕ} parameter since the constraints on $f_{\rm NL}b_{\phi}$ do not require priors on b_{ϕ} . The exercise on the right panel of Fig. 2 can be repeated for any observed galaxy sample by splitting it into two according to any measured galaxy property, and checking the improvements on the $f_{\rm NL}b_{\phi}$ constraints. Simulations can nonetheless still aid in this exploration through characterization of trends in b_1 and b_{ϕ} as a function of galaxy selection criteria. For example, should some suite of different galaxy formation models consistently predict that splits by property P yield larger values of $|b_1^B b_{\phi}^A - b_1^A b_{\phi}^B|$, then this motivates splits based on P to construct multi-tracer samples, even if the different models do not predict exactly the same values of $|b_1^B b_{\phi}^A - b_1^A b_{\phi}^B|$. From Fig. 2 we identify from the IllustrisTNG model that splits by color or stellar mass are a promising strategy to improve the SoD of $f_{\rm NL}$, but we caution that whether this holds also for other galaxy formation models is still unknown.

4 The impact of priors on b_{ϕ}

The discussion in the previous section shows that there is room to improve the probability to detect $f_{\rm NL}b_{\phi}$ that is not as affected by our ability to *precisely* predict the b_{ϕ} parameter of real galaxies. However, ultimately we are interested in either the numerical value or upper bounds on $f_{\rm NL}$ to draw more decisive conclusions about inflation. If b_{ϕ} is exactly known, the ratio of the $f_{\rm NL}$ precision for

³Note that our q-r split is not equal to the traditional split into star-forming (blue) and quiescent (red) galaxies.

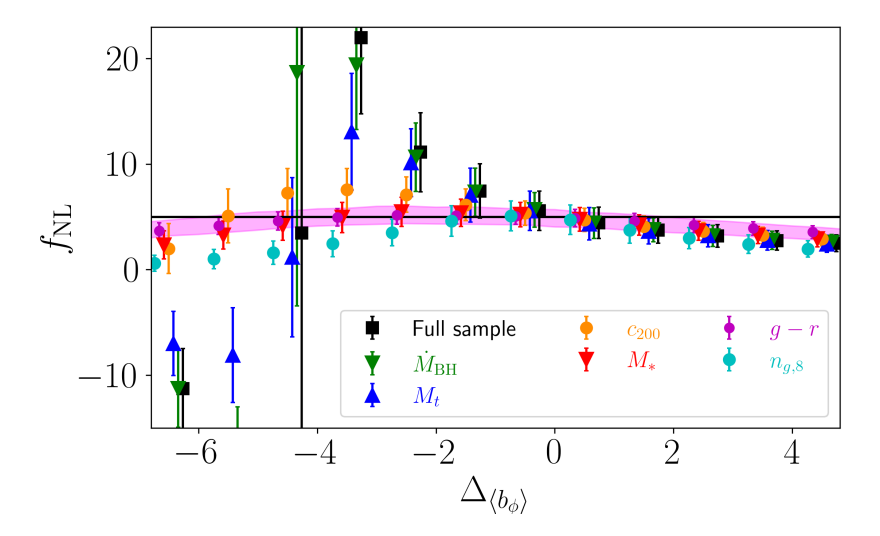


Figure 3. Impact of a systematic offset $\Delta_{\langle b_{\phi} \rangle}$ between the assumed and true values of b_{ϕ} on $f_{\rm NL}$ constraints. The different symbols/colors are for the different samples we consider in this work, as labeled. The magenta band simply marks the 1σ uncertainty region for the (g-r) multi-tracer split, which is the most robust to $\Delta_{\langle b_{\phi} \rangle}$. At a given $\Delta_{\langle b_{\phi} \rangle}$, the symbols are shifted horizontally for visualization; e.g., the third cluster of symbols from the left are all for $\Delta_{\langle b_{\phi} \rangle} = -4.5$, which is the b_{ϕ} zero-crossing of the full galaxy sample.

multi-tracer and single-tracer analyses $\sigma_{f_{\rm NL}}^{\rm MT}/\sigma_{f_{\rm NL}}^{\rm ST}$ is the inverse of the SoD ratio on the right of Fig. 2. This is not the case in reality, however, where calibration methods for b_{ϕ} (e.g. based on simulations [22–28]) are expected to come with some associated systematic offset and uncertainty.

In this section, we discuss the impact of priors on b_{ϕ} in single-tracer and multi-tracer $f_{\rm NL}$ constraints (see Refs. [26, 29, 38] for previous discussions for the single-tracer case). The results here are based on simulated likelihood analyses, i.e., we do not work with Fisher matrix forecasts to be able to quantify the impact of b_{ϕ} misspecifications on both the mean and error bar of the $f_{\rm NL}$ constraints. We keep assuming a fictitious survey with $V_S = 100~{\rm Gpc}^3/h^3$ at z = 1.

4.1 The impact of systematic offsets in b_{ϕ}

We start with the case where b_{ϕ} is precisely but inaccurately known, i.e., we investigate the impact of a systematic offset $\Delta_{\langle b_{\phi} \rangle}$ defined as $b_{\phi}^{A,B} = \langle b_{\phi} \rangle^{A,B} + \Delta_{\langle b_{\phi} \rangle}$, where $\langle b_{\phi} \rangle$ is the true value of the samples. We assume for simplicity the same offset $\Delta_{\langle b_{\phi} \rangle}$ for the sub-samples A,B in multi-tracer and for the full sample in single-tracer. Figure 3 shows the impact of $\Delta_{\langle b_{\phi} \rangle}$ on the $f_{\rm NL}$ constraints for the simulation-inspired galaxy selections of Fig. 2. The single-tracer result displays biased $f_{\rm NL}$ constraints that follow the expectation $f_{\rm NL} = \langle f_{\rm NL} \rangle \langle b_{\phi} \rangle / \left(\langle b_{\phi} \rangle + \Delta_{\langle b_{\phi} \rangle} \right)$, where $\langle f_{\rm NL} \rangle = 5$ is the true value. In particular, the constraints diverge when $\Delta_{\langle b_{\phi} \rangle} = \langle b_{\phi} \rangle = -4.5$. The critical impact of systematic offsets like $\Delta_{\langle b_{\phi} \rangle}$ in single-tracer constraints using BOSS DR12 galaxy data has been recently investigated in Ref. [30].

In contrast, the multi-tracer constraints appear more robust to $\Delta_{\langle b_{\phi} \rangle}$. While for $\Delta_{\langle b_{\phi} \rangle} > 0$ the impact is similar for multi-tracer and single-tracer, the multi-tracer constraints are visibly more robust to $\Delta_{\langle b_{\phi} \rangle} < 0$. The degree of robustness depends on the type of multi-tracer split, with the result in Fig. 3 displaying a rough correlation with the value of $|b_1^B b_{\phi}^A - b_1^A b_{\phi}^B|$. The splits by g - r, M_* and c_{200} are the most robust, being effectively unbiased on the range $-6 \lesssim \Delta_{\langle b_{\phi} \rangle} \lesssim 1$. In contrast, the

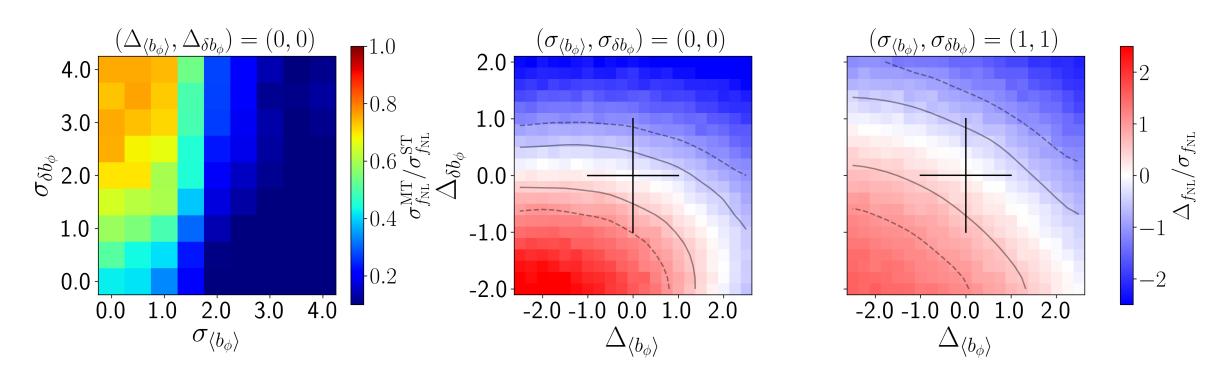


Figure 4. Left: relative constraining power of multi- vs. single-tracer analyses $\sigma_{f_{\rm NL}}^{\rm MT}/\sigma_{f_{\rm NL}}^{\rm ST}$ as a function of b_ϕ uncertainties, in the absence of systematic offsets. Middle, right: relative bias $\Delta f_{\rm NL}/\sigma_{f_{\rm NL}}$ as a function of systematic offsets in b_ϕ , for two different b_ϕ uncertainties as labeled. The solid, dashed contours indicate $\Delta f_{\rm NL}/\sigma_{f_{\rm NL}}=0.5,1$, respectively. For guidance, the black cross marks unity deviations from the origin $(\Delta_{\langle b_\phi \rangle},\Delta_{\delta b_\phi})=(0,0)$. The results in this figure are for the (g-r) multi-tracer case.

splits by $\dot{M}_{\rm BH}$ and M_t perform closer to the single-tracer result.

4.2 Exploration of multi-tracer b_{ϕ} prior requirements

In order to more realistically relate multi-tracer b_{ϕ} prior requirements to the single-tracer case, we consider now an extended parametrization of b_{ϕ} uncertainties. We denote by $b_{\phi}^{\rm ST}$ the value of the full sample, parametrize b_{ϕ} for the two multi-tracer samples as

$$b_{\phi}^{A} = b_{\phi}^{ST} + \delta b_{\phi}, \quad b_{\phi}^{B} = b_{\phi}^{ST} - \delta b_{\phi}, \tag{4.2}$$

and allow for systematic offsets and uncertainties on both $b_{\phi}^{\rm ST}$ and δb_{ϕ} . This reflects the fact that astrophysical modeling uncertainties can manifest themselves in miscalibrations of the mean of the full sample, as well as the shifts in b_{ϕ} caused by the multi-tracer selection criteria. Concretely, we assume a Gaussian prior for $b_{\phi}^{\rm ST}$ with mean and standard deviation $(\mu, \sigma) = (b_{\phi}^{\rm ST} + \Delta_{\langle b_{\phi} \rangle}, \sigma_{\langle b_{\phi} \rangle})$, and the same for δb_{ϕ} with $(\mu, \sigma) = (\delta b_{\phi} + \Delta_{\delta b_{\phi}}, \sigma_{\delta b_{\phi}})$. In this subsection we only show results for the g-r multi-tracer split; we note that b_{ϕ} prior requirements should be set relative to the underlying constraining power on $f_{\rm NL}$, and so are by construction survey-, sample- and analysis-specific.

The left panel of Fig. 4 shows the impact on the $f_{\rm NL}$ precision of the prior widths $\sigma_{\langle b_{\phi} \rangle}$ and $\sigma_{\delta b_{\phi}}$; the colors indicate the ratio $\sigma_{f_{\rm NL}}^{\rm MT}/\sigma_{f_{\rm NL}}^{\rm ST}$ of the error bar in multi-tracer and single-tracer, and the result is at zero offset $\Delta_{\langle b_{\phi} \rangle} = \Delta_{\delta b_{\phi}} = 0$. While the b_{ϕ} uncertainty causes $\sigma_{f_{\rm NL}}$ to increase for both multi-and single-tracer, the level of degradation of multi-tracer is kept significantly smaller. In this specific test, $\sigma_{f_{\rm NL}}^{\rm ST}$ varies by a factor of ~ 15 across the plot, while $\sigma_{f_{\rm NL}}^{\rm MT}$ increases by only 10%; this causes

$$\widehat{f_{\rm NL}} = \langle f_{\rm NL} \rangle \frac{\langle b_{\phi}^A \rangle \left(\langle b_{\phi}^A \rangle + \Delta_{\langle b_{\phi} \rangle} \right) / \sigma_A^2 + \langle b_{\phi}^B \rangle \left(\langle b_{\phi}^B \rangle + \Delta_{\langle b_{\phi} \rangle} \right) / \sigma_B^2}{\left(\langle b_{\phi}^A \rangle + \Delta_{\langle b_{\phi} \rangle} \right)^2 / \sigma_A^2 + \left(\langle b_{\phi}^B \rangle + \Delta_{\langle b_{\phi} \rangle} \right)^2 / \sigma_B^2} \,. \tag{4.1}$$

This expression can be used to build some intuition about the robustness to $\Delta_{\langle b_{\phi} \rangle}$. For example, if b_{ϕ} is misspecified as zero in single-tracer analyses, then this would imply no constraining power on $f_{\rm NL}$. However, in multi-tracer analyses, even if $\Delta_{\langle b_{\phi} \rangle}$ leads to misspecifying one of the b_{ϕ} as zero, one can still constrain $f_{\rm NL}$ from the other sample (assuming $b_{\phi}^{A} \neq b_{\phi}^{B}$). Further, the robustness in Fig. 3 can be understood in terms of a cancellation of effects by the two samples A, B when the assumed b_{ϕ}^{A} and b_{ϕ}^{B} bracket zero (i.e. one is negative and the other positive), which for our samples happens when $\Delta_{\langle b_{\phi} \rangle} < 0$. More concretely, for some b_{ϕ} misspecifications the two samples shift $f_{\rm NL}$ in opposite directions, yielding unbiased constraints. In contrast for single-tracer, any misspecification of b_{ϕ} always leads to biased constraints.

⁴The log-likelihood from sample A is $-2\ln\mathcal{L}^A = \left(\langle f_{\rm NL}b_\phi^A\rangle - f_{\rm NL}\left(\langle b_\phi^A\rangle + \Delta_{\langle b_\phi\rangle}\right)\right)^2/\sigma_A^2$ with $\sigma_A \equiv \sigma_{f_{\rm NL}b_\phi^A}$, and similarly for the other sample with $A \leftrightarrow B$. Ignoring the correlation between the two samples, the joint likelihood is the product $\mathcal{L}^A\mathcal{L}^B$, which has the following maximum likelihood estimator (the brackets $\langle \rangle$ indicate true values)

the strong left-to-right gradient.⁵ Further, for our specific g-r multi-tracer setup, the uncertainty on δb_{ϕ} causes only minor degradation on the $f_{\rm NL}$ precision (note the parameter $\sigma_{\delta b_{\phi}}$ is only for the multi-tracer case). The apparent extra resilience to b_{ϕ} uncertainties provides yet another motivation for multi-tracer $f_{\rm NL}$ constraints. In this case, the left of Fig. 4 suggests that the b_{ϕ} prior requirements may be less strict compared to single-tracer, which is opposite to the naive expectation that they would be stricter by the need to calibrate more than one b_{ϕ} value.

The middle and right panels of Fig. 4 quantify relative biases $\Delta f_{\rm NL}/\sigma_{f_{\rm NL}}$ in $f_{\rm NL}$ estimates as a function of the systematic offset parameters $\Delta_{\langle b_{\phi} \rangle}$ and $\Delta_{\delta b_{\phi}}$; the middle panel is for zero uncertainty $(\sigma_{\langle b_{\phi} \rangle}, \sigma_{\delta b_{\phi}}) = (0,0)$, and the right panel is for $(\sigma_{\langle b_{\phi} \rangle}, \sigma_{\delta b_{\phi}}) = (1,1)$. For orientation, the row at $\Delta_{\delta b_{\phi}} = 0$ in the middle panel corresponds to the g-r (magenta) symbols in Fig. 3. The result shows that while certain extreme misspecifications of b_{ϕ} can lead to 2σ biases (e.g. $(\Delta_{\langle b_{\phi} \rangle}, \Delta_{\delta b_{\phi}}) \approx (-2.5, -2)$ in the middle panel), there is also a order unity region around the zero misspecification point (black cross) where the $f_{\rm NL}$ biases remain small. As expected, the b_{ϕ} prior requirements for $\Delta f_{\rm NL}/\sigma_{f_{\rm NL}}$ are more relaxed for the case with $(\sigma_{\langle b_{\phi} \rangle}, \sigma_{\delta b_{\phi}}) = (1, 1)$, mostly due to the degradation in constraining power. We stress again that our quantitative results are specific to our survey setup and simulation-inspired g-r multi-tracer split. Figure 4 serves nonetheless as an example for how to deduce b_{ϕ} prior requirements for future real data analyses.

5 Summary and Conclusions

We revisited the potential of the multi-tracer technique to improve constraints on f_{NL} using galaxy data. Using Fisher matrix and parameter sampling forecasts for an idealized survey, we (i) quantified the impact of galaxy selection criteria on the constraining power, and (ii) explored the robustness of multi- and single-tracer analyses to b_{ϕ} misspecifications and uncertainties. Our main takeaways are:

- For multi-tracer analyses with two sub-samples A, B the constraining power is $\propto |b_1^B b_\phi^A b_1^A b_\phi^B|$ [31] (cf. Fig. 1). This is different, and leads in general to better constraints, than the naive expectation $\propto |b_1^A b_1^B|$ based on universality-like relations $b_\phi \propto b_1$.
- Indeed, different equal-number multi-tracer splits in galaxy formation simulations can lead to markedly different $|b_1^B b_{\phi}^A b_1^A b_{\phi}^B|$. For IllustrisTNG galaxies, we find that splits based on g r color can more than double the significance of detection (SoD) of $f_{\rm NL} b_{\phi} \neq 0$ (cf. Fig. 2). This result follows explicitly from the fact that g r cuts do not satisfy universality-like relations.
- Importantly, this ability to improve the SoD does not require priors on b_{ϕ} , and can even be pursed blindly by applying different multi-tracer splits according to any observed galaxy properties.
- Compared to single-tracer, multi-tracer $f_{\rm NL}$ constraints are also significantly more robust to b_{ϕ} misspecifications (cf. Fig. 3) and b_{ϕ} uncertainties (cf. Fig. 4). This provides extra incentive for multi-tracer analyses as a way to relax the requirements on b_{ϕ} priors from numerical simulations.

As future work, it would be interesting to study multi-tracer splits based on other galaxy properties, as well as to investigate how different astrophysics models compare in their b_1 , b_ϕ predictions. This is important to help identify which multi-tracer splits are most promising, as well as to calibrate b_ϕ priors. Our results motivate significantly investing in simulation campaigns towards improved chances to detect $f_{\rm NL} \neq 0$ and robustly constrain its value using multi-tracer galaxy data analyses.

Acknowledgments

We would like to thank Vincent Desjacques, Henry Gebhardt, Nick Kokron, Titouan Lazeyras and Fabian Schmidt for very useful comments and conversations. AB acknowledges support from the Excellence Cluster ORIGINS which is funded by the Deutsche Forschungsgemeinschaft (DFG, German

⁵Without prior information on b_{ϕ} , the likelihood in $\{f_{\rm NL}, b_{\phi}^A, b_{\phi}^B\}$ -space is constant along $f_{\rm NL}b_{\phi}=$ constant surfaces. Thus, there is a special direction along which $f_{\rm NL}$ can become arbitrarily large at fixed likelihood, and cannot therefore be constrained. The larger the number of $f_{\rm NL}b_{\phi}=$ constant surfaces, the more delicate this balance is, and so the easier it is to break by priors. This explains the extra robustness of multi-tracer relative to single-tracer analyses.

Research Foundation) under Germany's Excellence Strategy - EXC-2094-390783311. EK is supported in part by an Alfred P. Sloan Research Fellowship, the David and Lucile Packard Foundation, and the SPHEREx project under a contract from the NASA/GODDARD Space Flight Center to the California Institute of Technology. Part of this work is based on High-Performance Computing resources supported by the University of Arizona TRIF, UITS, and Research, Innovation, and Impact (RII) and maintained by the UArizona Research Technologies department

A Derivation of the Fisher information content in multi-tracer analyses

For a galaxy sample split into two sub-samples A and B, the Fisher information on f_{NL} is defined as

$$F_{f_{NL}}(k) = \frac{\partial \mathbf{D}^{t}(k)}{\partial f_{NL}} \cdot \mathbf{Cov}^{-1}(k) \cdot \frac{\partial \mathbf{D}(k)}{\partial f_{NL}}, \tag{A.1}$$

with the data vector given by

$$\mathbf{D}(k) = \left\{ P_{gg}^A(k), P_{gg}^{A \times B}(k), P_{gg}^B(k) \right\}, \tag{A.2}$$

and its covariance by (assuming only the contribution from the diagonal, disconnected piece)

$$\mathbf{Cov}(k) = 2\frac{(2\pi)^3}{V_s V_k} \begin{pmatrix} [P_{gg}^A(k)]^2 & P_{gg}^{A \times B}(k) P_{gg}^A(k) & [P_{gg}^{A \times B}(k)]^2 \\ \cdots & \frac{1}{2} \left[P_{gg}^A(k) P_{gg}^B(k) + [P_{gg}^{A \times B}(k)]^2 \right] P_{gg}^B(k) P_{gg}^{A \times B}(k) \\ \cdots & \cdots & [P_{gg}^B(k)]^2 \end{pmatrix} . \tag{A.3}$$

Rather than directly evaluating Eq. (A.1), we perform a few intermediate derivation steps as in Ref. [31] to help to highlight the origin of the power of the multi-tracer approach. The power spectra in Eq. (A.2) can be expressed as

$$\begin{split} P_{gg}^{A}(k,z) &= R(k)^{2} f^{B}(k)^{2} P_{mm}(k) + P_{\epsilon}^{A}, \\ P_{gg}^{A \times B}(k,z) &= R(k) f^{B}(k)^{2} P_{mm}(k), \\ P_{gg}^{B}(k,z) &= f^{B}(k)^{2} P_{mm}(k) + P_{\epsilon}^{B}, \end{split} \tag{A.4}$$

where

$$f^{A}(k) = b_{1}^{A} + f_{NL}b_{\phi}^{A}\mathcal{M}(k)^{-1},$$

$$f^{B}(k) = b_{1}^{B} + f_{NL}b_{\phi}^{B}\mathcal{M}(k)^{-1},$$

$$R(k) = \frac{f^{A}(k)}{f^{B}(k)}.$$
(A.5)

Note that the quantity R(k) measures the ratio of the deterministic (i.e. cosmological, or non-stochastic) parts of the galaxy power spectrum. As pointed out in the original multi-tracer discussion of Ref. [31], the power of the multi-tracer formalism relies in the observation that in the cosmic variance limit (small P_{ϵ}) the quantity R can be measured with infinite precision, and thus so can in principle any other parameter that R depends on, including $f_{\rm NL}$. Under the parametrization of Eq. (A.4) the data vector depends only on the variables R and f^{B} , and the Fisher information can be expressed as

$$F_{f_{NL}} = \sum_{\lambda,\lambda'=R,f^B} \frac{\partial \lambda}{\partial f_{NL}} F_{\lambda\lambda'} \frac{\partial \lambda'}{\partial f_{NL}}$$

$$= F_R \left(\frac{\partial R}{\partial f_{NL}}\right)^2 + F_{f^B} \left(\frac{\partial f^B}{\partial f_{NL}}\right)^2 + 2F_{R,f^B} \left(\frac{\partial R}{\partial f_{NL}}\right) \left(\frac{\partial f^B}{\partial f_{NL}}\right), \tag{A.6}$$

where F_R , F_{f^B} and F_{F,f^B} are, respectively, the Fisher information on R, f^B and their cross term. These are given by

$$F_{R} = 2 \frac{V_{S}V_{k}}{2(2\pi)^{3}} \frac{X^{A} + X^{B} + X^{A}X^{B} + 2(X^{B})^{2}}{R^{2}(X^{A} + X^{B} + X^{A}X^{B})^{2}}$$

$$F_{f_{B}} = 4 \frac{V_{S}V_{k}}{2(2\pi)^{3}} \frac{(X^{A} + X^{B})^{2}}{(f^{B})^{2}(X^{A} + X^{B} + X^{A}X^{B})^{2}}$$

$$F_{R,f_{B}} = 4 \frac{V_{S}V_{k}}{2(2\pi)^{3}} \frac{X^{B}(X^{A} + X^{B})}{Rf^{B}(X^{A} + X^{B} + X^{A}X^{B})^{2}}$$
(A.7)

The key observation is that, in the cosmic variance limit $X_A, X_B \to 0$, the Fisher information on F_R diverges as

$$F_R \longrightarrow 2 \frac{V_S V_k}{2(2\pi)^3} \frac{1}{R^2 (X^B + X^A)},$$
 (A.8)

while F_{f^B} and F_{R,f^B} asymptote to a constant. In this limit the power spectra of samples A and B is effectively deterministic and their ratio can be measured perfectly as both samples formed out of the same realization of the initial density field. From Eq. (A.6) we thus have in this limit that

$$F_{f_{\text{NL}}} \longrightarrow 2 \frac{V_S V_k}{2(2\pi)^3} \frac{1}{X^B + X^A} \left(\frac{\left(b_1^B b_\phi^A - b_1^A b_\phi^B \right) \mathcal{M}(k)^{-1}}{R(f^B)^2} \right)^2 + \mathcal{O}\left(X^A, X^B \right),$$
 (A.9)

which matches Eq. (2.7). As discussed in the main body of the paper, this equation tells us that, in the cosmic variance limit, the information content on $f_{\rm NL}$ increases with $\left|b_1^B b_\phi^A - b_1^A b_\phi^B\right|$, which is why multi-tracer splits that maximize this quantity can return better constraints on $f_{\rm NL}$.

References

- [1] E. Komatsu and D. N. Spergel, "Acoustic signatures in the primary microwave background bispectrum," *Phys. Rev. D* **63** no. 6, (Mar., 2001) 063002-+, arXiv:astro-ph/0005036.
- [2] J. Maldacena, "Non-gaussian features of primordial fluctuations in single field inflationary models," Journal of High Energy Physics 5 (May, 2003) 13, arXiv:astro-ph/0210603.
- [3] P. Creminelli and M. Zaldarriaga, "A single-field consistency relation for the three-point function," JCAP 2004 no. 10, (Oct., 2004) 006, arXiv:astro-ph/0407059 [astro-ph].
- [4] P. Creminelli, G. D'Amico, M. Musso, and J. Noreña, "The (not so) squeezed limit of the primordial 3-point function," *JCAP* **2011** no. 11, (Nov., 2011) 038, arXiv:1106.1462 [astro-ph.CO].
- [5] T. Tanaka and Y. Urakawa, "Dominance of gauge artifact in the consistency relation for the primordial bispectrum," JCAP 1105 (2011) 014, arXiv:1103.1251 [astro-ph.CO].
- [6] E. Pajer, F. Schmidt, and M. Zaldarriaga, "The Observed Squeezed Limit of Cosmological Three-Point Functions," *ArXiv e-prints* (May, 2013), arXiv:1305.0824 [astro-ph.CO].
- [7] O. Doré, J. Bock, M. Ashby, P. Capak, A. Cooray, R. de Putter, T. Eifler, N. Flagey, Y. Gong, and S. Habib, "Cosmology with the SPHEREX All-Sky Spectral Survey," arXiv e-prints (Dec, 2014) arXiv:1412.4872, arXiv:1412.4872 [astro-ph.CO].
- [8] M. Biagetti, "The Hunt for Primordial Interactions in the Large-Scale Structures of the Universe," *Galaxies* 7 no. 3, (Aug., 2019) 71, arXiv:1906.12244 [astro-ph.CO].
- [9] A. Achúcarro and et al, "Inflation: Theory and Observations," arXiv e-prints (Mar., 2022) arXiv:2203.08128, arXiv:2203.08128 [astro-ph.CO].
- [10] Planck Collaboration, "Planck 2018 results. IX. Constraints on primordial non-Gaussianity," Astron. Astrophys. 641 (Sept., 2020) A9, arXiv:1905.05697 [astro-ph.CO].

- [11] A. Slosar, C. Hirata, U. Seljak, S. Ho, and N. Padmanabhan, "Constraints on local primordial non-Gaussianity from large scale structure," *JCAP* 8 (Aug., 2008) 31—+, arXiv:0805.3580.
- [12] P. McDonald, "Primordial non-Gaussianity: Large-scale structure signature in the perturbative bias model," *Phys. Rev. D* **78** no. 12, (Dec., 2008) 123519—+, arXiv:0806.1061.
- [13] T. Giannantonio and C. Porciani, "Structure formation from non-Gaussian initial conditions: Multivariate biasing, statistics, and comparison with N-body simulations," *Phys. Rev. D* 81 no. 6, (Mar., 2010) 063530-+, arXiv:0911.0017.
- [14] T. Baldauf, U. Seljak, and L. Senatore, "Primordial non-Gaussianity in the bispectrum of the halo density field," *Journal of Cosmology and Astro-Particle Physics* 2011 (Apr., 2011) 006, arXiv:1011.1513 [astro-ph.CO].
- [15] V. Assassi, D. Baumann, and F. Schmidt, "Galaxy bias and primordial non-Gaussianity," JCAP 12 (Dec., 2015) 043, arXiv:1510.03723.
- [16] V. Desjacques, D. Jeong, and F. Schmidt, "Large-scale galaxy bias," Phys. Rep. 733 (Feb., 2018) 1-193, arXiv:1611.09787.
- [17] N. Dalal, O. Doré, D. Huterer, and A. Shirokov, "Imprints of primordial non-Gaussianities on large-scale structure: Scale-dependent bias and abundance of virialized objects," *Phys. Rev. D* 77 no. 12, (June, 2008) 123514-+, arXiv:0710.4560.
- [18] E.-M. Mueller and et al, "The clustering of galaxies in the completed SDSS-IV extended Baryon Oscillation Spectroscopic Survey: Primordial non-Gaussianity in Fourier Space," arXiv e-prints (June, 2021) arXiv:2106.13725, arXiv:2106.13725 [astro-ph.CO].
- [19] E. Castorina, N. Hand, U. Seljak, F. Beutler, C.-H. Chuang, C. Zhao, H. Gil-Marín, W. J. Percival, A. J. Ross, P. D. Choi, K. Dawson, A. de la Macorra, G. Rossi, R. Ruggeri, D. Schneider, and G.-B. Zhao, "Redshift-weighted constraints on primordial non-Gaussianity from the clustering of the eBOSS DR14 quasars in Fourier space," JCAP 2019 no. 9, (Sep, 2019) 010, arXiv:1904.08859 [astro-ph.CO].
- [20] G. D'Amico, M. Lewandowski, L. Senatore, and P. Zhang, "Limits on primordial non-Gaussianities from BOSS galaxy-clustering data," arXiv e-prints (Jan., 2022) arXiv:2201.11518, arXiv:2201.11518 [astro-ph.CO].
- [21] G. Cabass, M. M. Ivanov, O. H. E. Philcox, M. Simonović, and M. Zaldarriaga, "Constraints on multifield inflation from the BOSS galaxy survey," *Phys. Rev. D* **106** no. 4, (Aug., 2022) 043506, arXiv:2204.01781 [astro-ph.CO].
- [22] B. A. Reid, L. Verde, K. Dolag, S. Matarrese, and L. Moscardini, "Non-Gaussian halo assembly bias," JCAP 2010 no. 7, (July, 2010) 013, arXiv:1004.1637 [astro-ph.CO].
- [23] M. Biagetti, T. Lazeyras, T. Baldauf, V. Desjacques, and F. Schmidt, "Verifying the consistency relation for the scale-dependent bias from local primordial non-Gaussianity," Mon. Not. R. Astron. Soc. 468 no. 3, (Jul, 2017) 3277–3288, arXiv:1611.04901 [astro-ph.CO].
- [24] A. Barreira, G. Cabass, F. Schmidt, A. Pillepich, and D. Nelson, "Galaxy bias and primordial non-Gaussianity: insights from galaxy formation simulations with IllustrisTNG," JCAP 2020 no. 12, (Dec., 2020) 013, arXiv:2006.09368 [astro-ph.CO].
- [25] R. Voivodic and A. Barreira, "Responses of Halo Occupation Distributions: a new ingredient in the halo model & the impact on galaxy bias," *JCAP* **05** (2021) 069, arXiv:2012.04637 [astro-ph.CO]
- [26] A. Barreira, "Predictions for local PNG bias in the galaxy power spectrum and bispectrum and the consequences for $f_{\rm NL}$ constraints," JCAP **2022** no. 1, (Jan., 2022) 033, arXiv:2107.06887 [astro-ph.CO].
- [27] A. Barreira, "The local PNG bias of neutral Hydrogen, H_I," JCAP 2022 no. 4, (Apr., 2022) 057, arXiv:2112.03253 [astro-ph.CO].
- [28] T. Lazeyras, A. Barreira, F. Schmidt, and V. Desjacques, "Assembly bias in the local PNG halo bias and its implication for f_{NL} constraints," JCAP 2023 no. 1, (Jan., 2023) 023, arXiv:2209.07251 [astro-ph.CO].
- [29] A. Barreira, "On the impact of galaxy bias uncertainties on primordial non-Gaussianity constraints," JCAP 2020 no. 12, (Dec., 2020) 031, arXiv:2009.06622 [astro-ph.CO].

- [30] A. Barreira, "Can we actually constrain $f_{\rm NL}$ using the scale-dependent bias effect? An illustration of the impact of galaxy bias uncertainties using the BOSS DR12 galaxy power spectrum," JCAP 2022 no. 11, (Nov., 2022) 013, arXiv:2205.05673 [astro-ph.C0].
- [31] U. Seljak, "Extracting Primordial Non-Gaussianity without Cosmic Variance," Phys. Rev. Lett. 102 no. 2, (Jan, 2009) 021302, arXiv:0807.1770 [astro-ph].
- [32] T. Mergulhão, H. Rubira, R. Voivodic, and L. R. Abramo, "The effective field theory of large-scale structure and multi-tracer," *JCAP* **2022** no. 4, (Apr., 2022) 021, arXiv:2108.11363 [astro-ph.CO].
- [33] T. Mergulhão, H. Rubira, and R. Voivodic, "The Effective Field Theory of Large-Scale Structure and Multi-tracer II: redshift space and realistic tracers," arXiv e-prints (June, 2023) arXiv:2306.05474, arXiv:2306.05474 [astro-ph.CO].
- [34] A. Lewis, A. Challinor, and A. Lasenby, "Efficient Computation of Cosmic Microwave Background Anisotropies in Closed Friedmann-Robertson-Walker Models," *Astrophys. J.* 538 (Aug., 2000) 473–476, astro-ph/9911177.
- [35] E. Castorina, Y. Feng, U. Seljak, and F. Villaescusa-Navarro, "Primordial Non-Gaussianities and Zero-Bias Tracers of the Large-Scale Structure," *Phys. Rev. Lett.* 121 no. 10, (Sept., 2018) 101301, arXiv:1803.11539 [astro-ph.CO].
- [36] A. Pillepich, V. Springel, D. Nelson, S. Genel, J. Naiman, R. Pakmor, L. Hernquist, P. Torrey, M. Vogelsberger, R. Weinberger, and F. Marinacci, "Simulating galaxy formation with the IllustrisTNG model," *Mon. Not. R. Astron. Soc.* 473 no. 3, (Jan., 2018) 4077-4106, arXiv:1703.02970 [astro-ph.GA].
- [37] S. Alam, Y. Zu, J. A. Peacock, and R. Mandelbaum, "Cosmic web dependence of galaxy clustering and quenching in SDSS," Mon. Not. R. Astron. Soc. 483 no. 4, (Mar., 2019) 4501-4517, arXiv:1801.04878 [astro-ph.CO].
- [38] A. Moradinezhad Dizgah, M. Biagetti, E. Sefusatti, V. Desjacques, and J. Noreña, "Primordial non-Gaussianity from biased tracers: likelihood analysis of real-space power spectrum and bispectrum," *JCAP* **2021** no. 5, (May, 2021) 015, arXiv:2010.14523 [astro-ph.CO].